J. Fluid Mech. (1997), *vol.* 351, *pp.* 75–103. Printed in the United Kingdom

Inviscid dipole-vortex rebound from a wall or coast

By G. F. CARNEVALE[1], O. U. VELASCO FUENTES[2] AND P. ORLANDI[3]

[1]Scripps Institution of Oceanography, University of California, San Diego, La Jolla, CA 92093-0225, USA

[2]Centro de Investigacion Cientifica y de Educacion Superior de Ensenada, 22800 Ensenada, Baja California, Mexico

[3]Department of Mechanics and Aeronautics, University of Rome "La Sapienza," via Eudossiana 18, 00184 Rome, Italy

(Received 16 November 1996 and in revised form 30 June 1997)

A vortex approaching a no-slip wall 'rebounds' due to the creation of vorticity at the wall in a viscous boundary layer. Here it is demonstrated that a purely inviscid mechanism can also produce vortex rebound from a slip wall. In inviscid vortex rebound, vortex tube stretching generates the necessary vorticity to allow rebound, eliminating the need for viscous vorticity generation. This vortex stretching mechanism is demonstrated through numerical simulations and laboratory experiments on dipole-vortex rebound from a boundary. In an application to oceanography, numerical simulations of both quasi-geostrophic and shallow water dynamics are used to show that the β-effect at an eastern boundary can produce this inviscid rebound. Through a series of numerical experiments in which the strength of the β-effect is varied, a formula for predicting the point of separation of the vortices from the boundary in a dipole–coast collision is deduced. Through simulations, the flux of vorticity and fluid away from the boundary is measured as a function of β and initial angle of incidence. It is found that, in contrast to viscous vortex rebound, which typically does not produce a flux of material away from the boundary farther than a distance comparable to the initial vortex radius, the β-induced rebound does carry fluid far from the coast. Laboratory experiments in a rotating tank are used to show that a sloping bottom can also provide an inviscid mechanism for dipole-vortex rebound from the wall of the tank under certain conditions. A relation determining the conditions under which inviscid or viscous processes will dominate in the rebound of the dipole from a boundary is obtained.

1. Introduction

In vortex rebound, a vortex approaching a wall is forced away by the influence of the secondary flow induced by the vortex in the presence of a wall. This process is of importance in both engineering and oceanography. In engineering applications, rebound is due to the creation of vorticity in a viscous boundary layer at a wall with the no-slip condition. Rebound is possible, however, even in cases in which the boundary is taken to be a slip wall, which does not support viscous generation of vorticity. We will show that in oceanographic applications there

are inviscid sources of vorticity which can cause rebound even on a coast modelled by a slip boundary condition. In laboratory experiments on the flow in a rotating tank, we will demonstrate inviscid rebound in the presence of a sloping bottom.

In the viscous rebound problem, as a vortex approaches the wall, the viscous boundary layer that it creates grows in strength. The vorticity created in this boundary layer has sign opposite to that in the primary vortex. The flow induced by this boundary layer vorticity can carry the primary vortex away from the wall. This process was the subject of a number of experimental studies starting with Harvey & Perry (1971). More recently, van Heijst & Flor (1989) studied the rebound of a dipolar vortex in a stratified fluid. Orlandi (1990) studied the problem of dipole rebound from a no-slip wall numerically and successfully reproduced the laboratory results of van Heijst & Flor (1989). Perhaps the simplest model of a vortex approaching and interacting with a wall is the dipole–wall interaction. The dipole, in particular the Lamb dipole (Lamb 1932), is an ideal model of a propagating vortex since, in the absence of boundaries, it propagates at constant speed without changing direction. Thus by having the vortex trajectory intersect a wall, we can see effects produced solely by the presence of the wall, without the necessity of embedding the vortex in a more complicated external flow. Thus our study will focus on the dipole–wall interaction.

In the slip-wall problem, there is no viscous generation of vorticity at the wall. Indeed, in pure two-dimensional inviscid flow, a dipole colliding with a wall will split with the oppositely signed vortices simply moving in opposite directions along the wall (cf. Saffman 1979). In coastal dynamics, however, the principle of potential vorticity conservation allows inviscid relative-vorticity creation. For example, the curvature of the Earth's surface gives rise to the β-effect (cf. Pedlosky 1987), which, as we will show, will allow the rebound of a dipole from a coast. This simple example can be used as a model for the effects that also can be expected for more complicated vortex stretching mechanisms. Typically, topographic variations and the variation of iso-levels of density will stretch or compress vortex columns as they approach a coast. These effects will produce results more complicated than simple vortex rebound; however, the important elements involved will already be seen in the simple β-plane problem on which we will concentrate. In reality, there will be a competition between inviscid and viscous processes during a vortex–coast interaction. The extent to which one process will dominate over the other is also explored here.

Through numerical simulations and laboratory experiments, we have investigated the effects of β and topographic stretching on a dipole approaching a wall. In this paper, the similarities and differences between viscous and inviscid rebound are discussed. Section 2 is a review of various aspects of the viscous rebound problem, providing a background for our discussion of the inviscid rebound work. In §3, we demonstrate the possibility of inviscid rebound through numerical experiments. Specifically, we consider the case of a dipolar vortex approaching an eastern boundary and explore the role of the β-effect in vortex rebound. We are able to give a quantitative relationship predicting the point at which the vortices of the dipole will leave the coast. In §4, we show that the amount of fluid transported away from a coast during vortex rebound can be very different depending on whether viscous or inviscid processes dominate. Our numerical predictions have been compared successfully to laboratory experiments in a rotating tank. In these experiments, discussed in §5, the β-effect is simulated by a sloping bottom such that there is a topographic gradient parallel to the coast. Finally, in section §6, we consider the effect of a topographic gradient perpendicular to the coast.

2. Viscous rebound

Orlandi (1990) studied the problem of a dipole colliding with a no-slip wall at a right-angle of incidence. This was a numerical study based on simulations of the advection of relative vorticity subject to Laplacian lateral diffusion. The evolution equation is

$$\frac{\partial \omega}{\partial t} + J(\psi, \omega) = \nu \nabla^2 \omega, \tag{2.1}$$

where vorticity ω and streamfunction ψ are related through the Poisson equation: $\omega = \nabla^2 \psi$.

We use a finite-difference numerical scheme to simulate this equation. This is a streamfunction–vorticity scheme using the Arakawa (1966) method for computing the Jacobian in an energy and enstrophy conserving manner. For time stepping, we use a third-order Runge–Kutta scheme that is efficient and sparing in memory allocation (cf. Rai & Moin 1991). The time step can either be fixed or allowed to vary subject to satisfaction of the CFL condition, that is with a CFL number of 1 (cf. Peyret & Taylor 1983). Boundary conditions can be set as either slip, no-slip, or radiation, depending on the application. The radiation condition, based on the Orlanski (1976) algorithm, updates the streamfunction and vorticity on the boundaries each time step. Once the vorticity in the domain is determined by time stepping the evolution equation, the streamfunction is determined in the interior by inverting the Poisson equation using the updated boundary values.

The dipole used as the initial condition is the Lamb dipole. This is an exact solution of the inviscid equations of motion on the infinite f-plane (cf. Lamb 1932; Batchelor 1967). In polar coordinates centred on the dipole, with $\theta = 0$ corresponding to the direction of propagation, the vorticity distribution is given by

$$\left.\begin{aligned} \omega = \omega_{int} &= -2Uk \frac{J_1(kr)}{J_0(ka)} \sin\theta \qquad (r \leqslant a), \\ = \omega_{ext} &= 0 \qquad\qquad\qquad\quad (r > a), \end{aligned}\right\} \tag{2.2}$$

and the streamfunction in the reference frame of the dipole is given by

$$\left.\begin{aligned} \psi = \psi_{int} &= \frac{2U}{k} \frac{J_1(kr)}{J_0(ka)} \sin\theta \qquad (r \leqslant a), \\ = \psi_{ext} &= U\left(-\frac{a^2}{r} + r\right) \sin\theta \qquad (r > a). \end{aligned}\right\} \tag{2.3}$$

Here U is the speed of propagation, a is the radius of the circle separating the 'interior' from the 'exterior' of the dipole, and k is a constant such that $ka = j_1^1 \approx 3.81$ is the first non-trivial zero of the Bessel function J_1. Note that this is a stationary solution in the co-moving reference frame. All vorticity is confined to the interior, and we have potential flow in the exterior region.

Note that from (2.3) the streamfunction in the stationary reference frame falls off as $1/r$ in the far field for the infinite domain. Thus the velocity falls off as $1/r^2$. For the initial value of ψ on the boundaries of the computational domain, we chose $\psi = 0$. Test runs in which we doubled the computational domain size showed little difference in the subsequent evolution. Apparently the decay in ψ given in (2.3) is sufficiently rapid that initially assigning $\psi = 0$ on the boundaries does not make a significant error given the size of our computational domain.

The type of boundary conditions maintained at the boundary plays a crucial role in determining the fate of an approaching vortex. Although the appropriate boundary

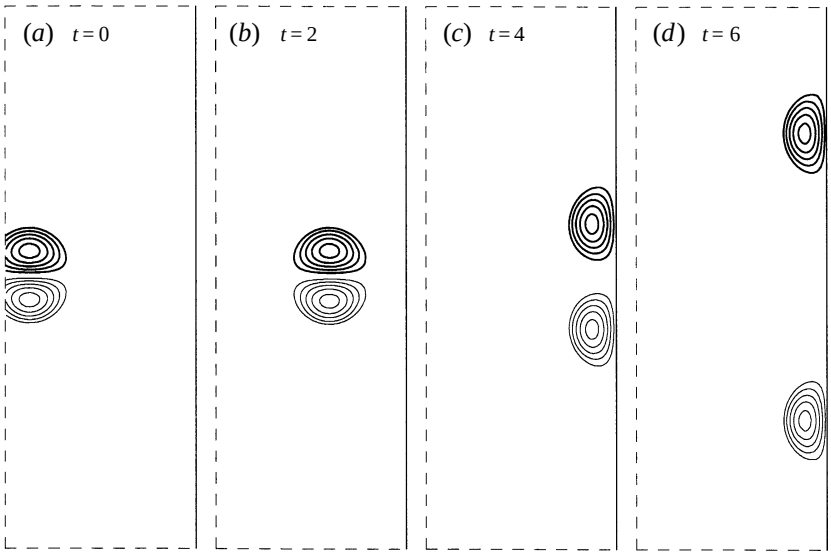

FIGURE 1. Inviscid simulation of a dipole colliding with a free-slip wall on the f-plane. Thin/thick lines represent levels of negative/positive vorticity. The zero vorticity level is not drawn, and the contour interval is $2U/a$ (see text). Time is given in advective time units, a/U. The simulation was performed assuming antisymmetry of the vorticity field about $y = 0$. The time step was $0.005a/U$. The grid-spacing in the $x(y)$-direction was $6a/257$ ($8a/257$). In the $x(y)$-direction only 60% (62.5%) of the computational domain is displayed.

condition at a solid surface is no-slip, that is, no flow through or along the boundary, there are circumstances in which the idealization of a slip wall is very useful. In modelling high-Reynolds-number large-scale flows in oceanography, it is not possible to fully resolve all scales of motion, and the small-scale processes near the coast are often poorly resolved or entirely neglected. We can imagine that the large-scale flow slips past the coastal zone where the small-scale processes provide a complicated transition to the flow that actually impinges on solid surface. In other words, we think of the solution as being composed of two parts: an outer solution with slip boundary condition and a complicated boundary layer with no-slip at solid surfaces (cf. Pond & Pickard 1978; Pedlosky 1996).

The condition of no normal flow alone leaves the vorticity on the boundary unspecified. If we consider the case with no viscosity, in the absence of any inviscid mechanism for vorticity creation, we have $\mathrm{D}\omega/\mathrm{D}t = 0$ everywhere, including the boundary. Thus ω on the boundary evolves through advection and needs to be tracked from the initial data and boundary values. If ω is initially zero on the boundary and there is no source of vorticity at the ends of the boundary (i.e. no imposed inlet condition for flow along the boundary), then ω will remain zero on the boundary (Roache 1982), and this is the appropriate boundary condition in the case we will next consider.

We begin by looking at the result of a dipole approaching a straight slip wall with $v = 0$. At time $t = 0$ in figure 1, the dipole is moving to the right toward a slip wall indicated by the solid boundary line. Only a portion of the computational domain is shown, and the dashed boundaries just indicate where the image has been cut off. After colliding with the wall, the two vortices separate and travel along the wall in opposite directions. This motion continues indefinitely. In the simulation, the vortices simply leave the computational domain through the radiation walls on

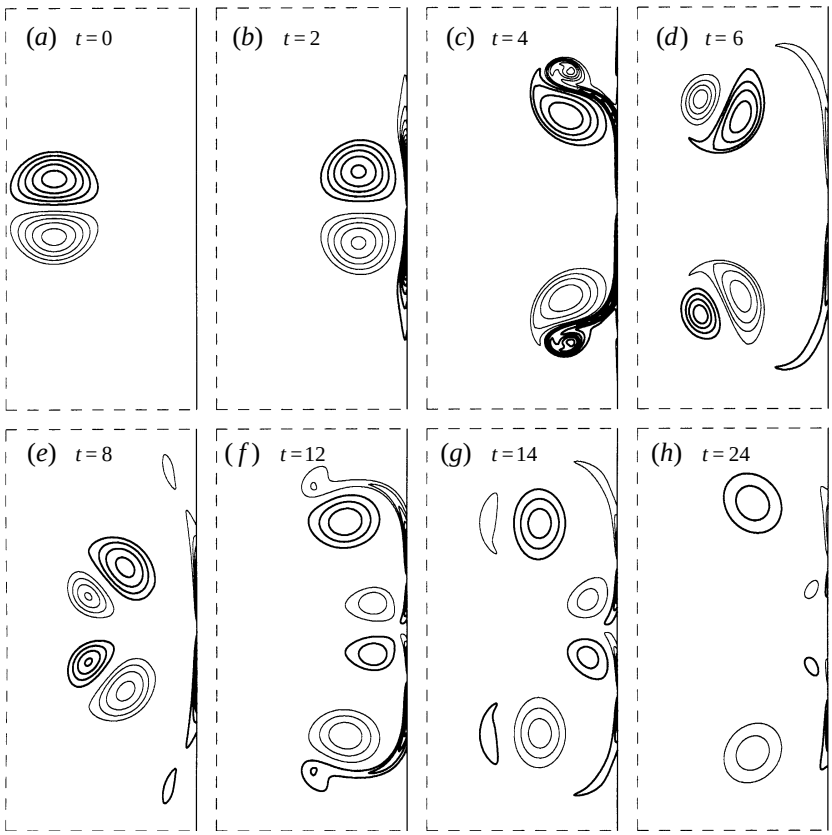

FIGURE 2. Viscous simulation of a dipole colliding with a no-slip wall. Thin/thick lines represent levels of negative/positive vorticity. Maximum and minimum contour levels were cut off at $\pm 2|\omega_0|$, where $|\omega_0|$ is the maximum vorticity of the initial condition. The zero vorticity level is not drawn. The Reynolds number of the flow is initially $Re \equiv Ua/\nu = 500$. Time is given in advective time units, a/U. The simulation was performed assuming antisymmetry of the vorticity field about $y = 0$. The grid-spacing was $0.02a$ in each direction. The time step was $0.01a/U$. Only 75% of the computational domain is displayed in each direction.

the top and bottom where we have applied the Orlanski (1976) radiation boundary conditions. One can consider this behaviour in terms of the theory of 'image charges' or 'image vortices.' From this point of view, the wall corresponds to a straight, constant, streamline which is maintained by the superposition of the fields induced by the real vortices and their images (reflections of oppositely signed vorticity) in the wall. Thus, as the dipole collides with the wall, each primary vortex forms a new dipole with its image vortex. The two new real+image pairs propagate like real dipoles which takes them in opposite directions along trajectories that hug the wall. No real vorticity is generated on any fluid particle during this evolution, and, after the collision, the vortices never again leave the wall.

In contrast to the inviscid slip problem, in a collision with a no-slip boundary, the vortices in the dipole actually rebound following their initial encounter with the wall. In figure 2, we show a low Reynolds number example of this viscous dipole rebound. Here we will define the Reynolds number of the flow as $Re = Ua/\nu$ where U is the speed of the dipole (which is the same order of magnitude as the fastest velocity in the frame moving with the dipole), and a is the dipole radius. At $t = 0$ the dipole is

moving from left to right, approaching the no-slip wall. As the dipole approaches the wall, it creates a flow near the wall in the direction parallel to the wall. Consequently a boundary layer forms, as we see in panel (*b*). Because of the direction of flow around each primary vortex, the vorticity created at the wall has sign opposite to that of the nearest approaching vortex. As the primary vortex gets closer, it begins to roll up the boundary layer, creating a vortex of vorticity with sign opposite to that of the primary vortex which created it. The combination of the secondary vortex and the primary vortex is a new dipole with a propagation direction pointed away from the wall, as we see in panel (*c*). Hence, the primary vortex is carried away from the wall. Once the vortex leaves the wall, the strength of the secondary vortex can no longer increase. Since the trajectory of this new dipole is an arc with the primary vortex on the inside, the strength or circulation of the secondary vortex is less than that of the primary vortex. The magnitude of the actual vorticity levels achieved near the wall in this simulation was more than six times larger than the original peak vorticity ω_0 of the dipole. We checked that the simulation illustrated in figure 2 was sufficiently well resolved with regard to the effects of the viscous boundary layer roll-up by running a simulation in which we more that doubled the resolution near the wall by shrinking the coordinate system near the wall. There were no significant differences in the two simulations either with regard to the boundary layer formation or the subsequent evolution. In figure 2, we cut off the contour levels with magnitude above $2\omega_0$ since the higher contour levels at the wall are too densely packed to resolve in these plots. Although high values of vorticity are achieved, the region that they occupy is relatively narrow, and the total circulation of the secondary vortex that results from the roll-up is less than the circulation of the primary vortex. Thus, each new dipole leaves the wall on a curving trajectory that eventually has the primary vortices return to the wall. This second approach to the wall again produces new vortices (tertiary) which again cause the primary vortices to rebound. Note that the secondary vortices have been left behind forming a dipole pointing away from the wall (see panel *f*). This dipole of secondary vortices is not strong enough to leave the wall, because near the *x*-axis there is a velocity field induced by the primary vortices that is strong enough to oppose the motion of the dipole of secondary vortices. This dipole just slowly decays in place as viscous dissipation diminishes the strength of all the vortices. Therefore, although there is rebound, the primary vortices and all subsequently created vortices remain relatively close to the wall as they slowly decay.

Interestingly, there is a small range of Reynolds number, approximately given by $1000 < Re < 2500$, in which the dipole of secondary vortices that we see pointing away from the wall in figure 2(*f*) (time $t = 12$) is reinforced during the return of the primaries and becomes strong enough to leave the wall. It then propagates indefinitely far from the wall taking wall fluid with it. Thus, in this range of Reynolds numbers, there is a flux of wall fluid away from the wall. For Reynolds numbers above this range (we have explored Reynolds numbers up to 5000), this reinforcement of the secondary vortices does not occur due to a difference in timing of the return of the primary vortices. Thus, there is no escape from the wall region and, hence, no significant flux of fluid away from the wall.

The position where the primary vortex leaves the wall appears to be only weakly dependent on the Reynolds number. The indication from theoretical and numerical work on boundary layer separation is that the infinite Reynolds number limit of the no-slip problem is very different from the inviscid problem with a slip boundary (Peridier, Smith & Walker 1991; Orlandi 1990, 1991). As the Reynolds number

increases, the distance the primary vortex moves along the boundary before separation or rebound approaches a finite limit of the order of the radius of the dipole.

3. Inviscid rebound

As noted in the introduction, in the interaction of an eddy with a coast, there are processes other than viscous boundary layer formation that can also produce relative vorticity. Vortex stretching due to the presence of topography, isopycnal height variations, and ambient potential vorticity variations provide inviscid sources of relative vorticity. The precise effect that these vorticity generation mechanisms will have on a vortex approaching a coast depends greatly on questions of geometry and orientation. It is our purpose here simply to illustrate some of the basic elements that make inviscid rebound possible.

As the simplest example of inviscid rebound, we have considered in some detail the result of a dipole approaching a coast with a slip boundary condition in the presence of the β-effect. The simplest model which incorporates this effect is the inviscid, quasi-geostrophic model for a single homogeneous fluid layer. The evolution equation in this model is (cf. Pedlosky 1987)

$$\frac{\partial \omega}{\partial t} + J(\psi, \omega + \beta y) = 0. \tag{3.1}$$

Here x is the coordinate for east-west translations and $y = R(\theta - \theta_0)$ represents meridional translations, on a sphere of radius R, centred on a reference latitude θ_0. The effective variation of the background rotation rate with latitude is represented by the β-term where $\beta = 2\Omega \cos\theta_0 / R$ (cf. Pedlosky 1987). According to this evolution equation, the potential vorticity $q \equiv \omega + \beta y$ is conserved following fluid particles. We consider the case of a vortex approaching an eastern boundary.

A form-preserving dipole can also exist on the β-plane. In fact, the Lamb dipole (equation (2.2)) is the $\beta = 0$ limit of a more general dipolar structure called the modon (Stern 1975; Larichev & Reznik 1976). The vorticity field of the modon in polar coordinates is given by

$$\left.\begin{aligned} \omega &= -\beta a \frac{J_1(\lambda r)}{J_1(\lambda a)} \sin\theta \qquad (r \leqslant a), \\ &= -\beta a \frac{K_1(\rho r)}{K_1(\rho a)} \sin\theta \qquad (r > a), \end{aligned}\right\} \tag{3.2}$$

where J_1 and K_1 are the first-order Bessel and modified Bessel functions, respectively. The radius a defines a circle which we can take as the border between the interior and exterior regions of the modon. The ratio $\rho = \beta / U$, where U is the forward speed, gives the exterior inverse length scale of the vorticity distribution. The angular variable θ is the polar coordinate defined so that $\theta = 0$ is the direction of propagation. The interior inverse length scale λ is derived from a dispersion relation which ensures the continuity of the tangential velocity at $r = a$. That dispersion relation is

$$\frac{-J_2(\lambda a)}{\lambda J_1(\lambda a)} = \frac{K_2(\rho a)}{\rho K_1(\rho a)}. \tag{3.3}$$

Once the modon's radius a and speed U are specified, the parameter λ is determined through (3.3). The dispersion relation has an infinity of branches, but the customary modon is the one corresponding to the branch with the lowest value of λ.

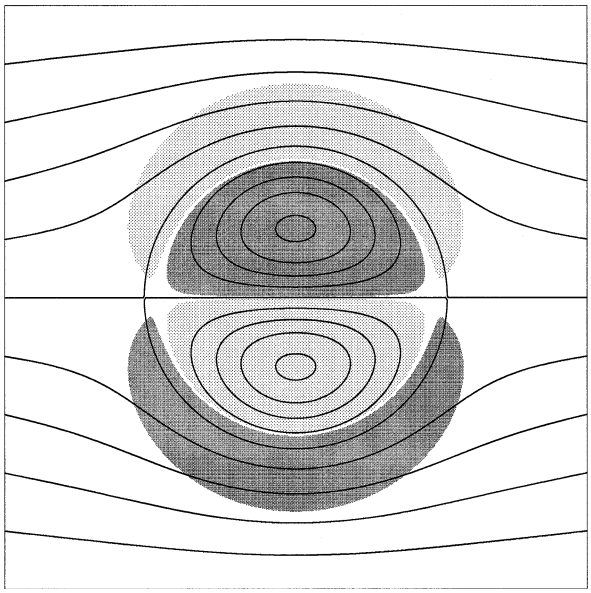

FIGURE 3. Vorticity and streamfunction for the $\beta = 4U/a^2$ modon. Streamlines are superimposed on the vorticity field. Dark/light shading represents positive/negative vorticity regions of amplitude greater than $0.5U/a$. The streamfunction contour increments are $0.4Ua$.

Unlike the case of the Lamb dipole, where the direction of propagation is arbitrary, propagation for the modon is exactly form-preserving only for motion due east, that is only when $\theta = 0$ corresponds to the east or the positive x-direction. Propagation in other directions results in variation of the strengths of the constituent vortices, and this results in deviations from straight-line motion. Furthermore, the eastward trajectory proves to be stable to small perturbations in direction. For the equivalent barotropic model, where effects of the evolution of free surface height are allowed, there also exists a westward propagating modon (Larichev & Reznik 1976), but in that case the trajectory is not stable (Nycander 1992), and the interaction with the coastline is rather different. We will confine ourselves solely to a discussion of the eastward propagating modon. Numerical investigations indicate that the basic dipolar form of the modon is stable to rather strong perturbations (cf. McWilliams *et al.* 1981). When the perturbations exceed a certain threshold, however, the structure can fission into separate vortices (cf. Carnevale *et al.* 1988*a*,*b*).

During the propagation of the modon, fluid particles are transported along with the modon and make closed circuits around the extrema of potential vorticity. When the motion of these particles carries them toward the north/south, their relative vorticity must decrease/increase in accordance with the law of potential vorticity conservation. This must all be done in such a way that the field of relative vorticity is constant in time in the co-moving reference frame. In figure 3, we show the streamfunction superimposed on the vorticity field in the co-moving frame for the case $\beta = 4U/a^2$. Note that the relative vorticity vanishes at a radius r such that $\lambda r = j_1^1$, where j_1^1 is the first zero of the Bessel function J_1. For non-zero β this radius is less than a, the radius of the modon. Thus, unlike the case of the Lamb dipole, here there is, besides the main vortex, a layer of oppositely signed vorticity that extends from the interior to the exterior of the modon. For the values of β that we are dealing with, the vorticity amplitude in this layer is small compared to the peak vorticity. Nevertheless,

this layer is necessary to allow for form-preserving propagation. To see this, consider a streamline in the northern half of the interior which comes very close to the x-axis. A particle starting near the x-axis on this streamline will have nearly zero relative vorticity. Thus, as this particle moves northward following closely the circle that defines the vortex radius, it must attain negative relative vorticity by potential vorticity conservation, hence, the necessity of the secondary lobe of oppositely signed vorticity.

We have performed numerical simulations of the approach of modons to straight slip coasts using spectral, finite-difference, and vortex-in-cell methods. Each method has its advantages. The finite-difference technique is attractive because of the ease with which various boundary conditions can be incorporated. The finite-difference numerical code that we use to simulate the approach of the vortex to a slip wall is the same as the one that we used in the viscous rebound problem except that we allow for flow along the coast. One of the disadvantages of finite-difference modelling is that even though we use a slip boundary we still need to maintain some viscosity to damp spurious small-scale motions. We set the value of the viscosity to a level such that the initial Reynolds number, defined as in the previous section, was 5000, which is small enough to keep the numerical solutions stable but large enough so that there is no significant loss of vorticity in the core of the primary vortices during the evolution period of interest. Whether or not there is explicit viscosity is not as important to our results as is the choice of slip or no-slip boundary conditions (Roache 1982). Even in the limit of vanishing viscosity, the choice of a no-slip boundary will allow the creation of strong vorticity at the boundary, producing flows very different from those with slip boundaries.

Since there is no flow normal to the coast, a particle on the slip boundary moving due to the alongshore velocity will have its vorticity defined by $\omega = \omega_0 - \beta(y - y_0)$, where y_0 is the initial position of the particle on the boundary and ω_0 is the particle's initial vorticity. For a finite-difference code, this type of Lagrangian boundary condition would be more difficult to simulate than a Eulerian-type boundary condition. We found it convenient to approximate vorticity on the eastern boundary by the condition $\partial\omega/\partial x = 0$ where x is in the direction normal to the wall. This is a reasonably good approximation to the slip condition because the flow just off the wall is subject to the same change in βy as the flow along the wall. Note also that the slip condition, by allowing the generation of vorticity on the wall will, in a code with viscosity, produce a viscous stress at the wall (cf. Landau & Lifshitz 1959, p. 58). To keep the flow at a straight wall free of viscous stresses would require keeping the vorticity zero at the wall. To test the sensitivity of our results to the choice of stress-free, $\omega = 0$, or our approximate slip boundary condition, $\partial\omega/\partial x = 0$, we compared the vortex trajectories using each of these boundary conditions and found no significant difference. The only noticeable difference appears to be in the viscous dissipation very close to the wall, and this proves to be an insignificant effect for our rebound problem. Also, as we shall discuss below, we further tested our results using the inviscid vortex-in-cell method with $\omega = 0$ on the boundary, and found no significant differences compared to our finite-difference results.

The evolution predicted by finite-difference simulation of the modon approach to a slip wall is illustrated for one case in figure 4. To improve resolution in this figure, we are representing only the northern half of the field. The evolution for the southern half is just a reflection in the symmetry axis of the initial modon, provided the signs of vorticity are also changed. In the figure, we see the cyclone of an eastward propagating modon approaching a straight eastern boundary. The contour levels are

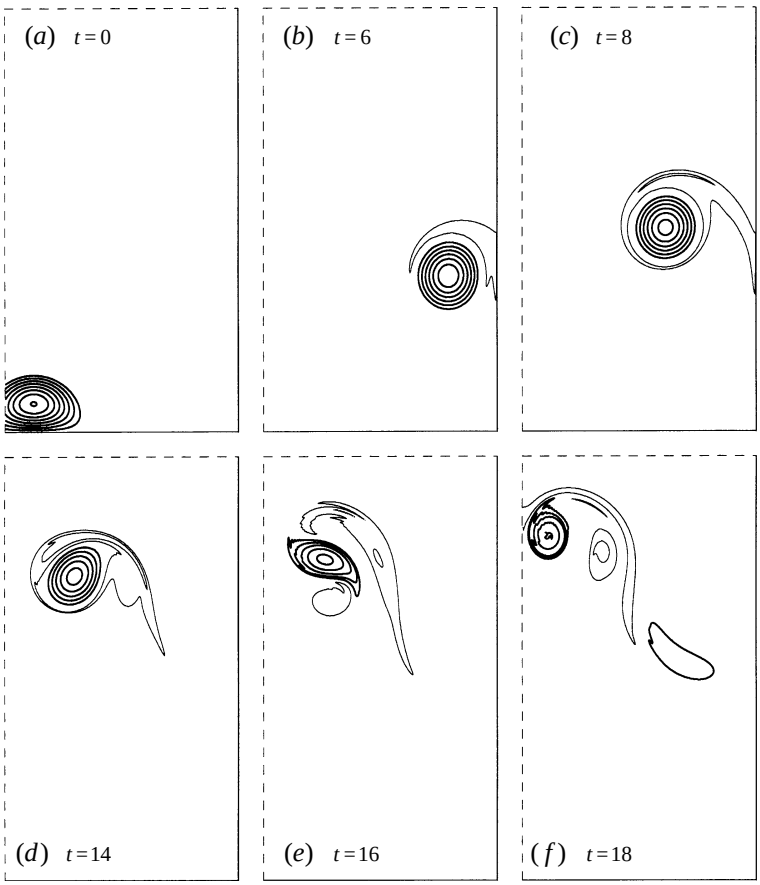

FIGURE 4. Vorticity contours illustrating the simulation of a modon colliding with a slip wall on a β-plane with $\beta = U/a^2$. Thin/thick lines represent levels of negative/positive vorticity. The zero vorticity level is not drawn. The Reynolds number of the flow is initially $Re \equiv Ua/\nu = 5000$. Time is given in advective time units, a/U. The simulation was performed assuming anti-symmetry of the vorticity field about $y = 0$. The time step was variable subject to the CFL condition (see text). The grid-spacing in the $x(y)$-direction was $0.012a$ ($0.016a$). In the $x(y)$-direction only 67% (94%) of the computational domain is displayed.

the same in all panels. For this case $\beta = 1$ and the contour interval is too large to show the thin, weak, outer layer of negative vorticity actually present in the modon at $t = 0$. As the cyclone reaches the wall, it is affected strongly by the image vorticity in the wall, and it moves northward along the wall. The field of the cyclone plus image anticyclone in the wall forces fluid directly northward along the wall. It is at this stage that rapid anticyclonic vorticity production begins (see figure 4*b*). As the cyclone moves northward, its vorticity decreases due to conservation of potential vorticity. Meanwhile, as the anticyclonic lobe that accompanies the cyclone moves north, the magnitude of *its* vorticity must increase. Eventually, the anticyclonic lobe becomes strong enough to advect the centre of the cyclone away from the wall. The farther the cyclone moves from the wall, the weaker is the influence of the image (anticyclonic) vortex in the wall, and hence the less important the presence of the wall. In fact, shortly after leaving the wall, the evolution of the cyclone resembles that of a cyclone on a β-plane without the influence of boundaries (cf. Carnevale,

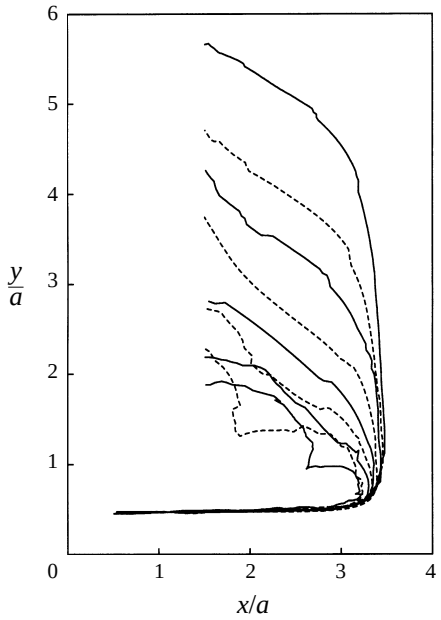

FIGURE 5. Trajectories of the peak of positive (cyclonic) relative vorticity for $\beta = 0.5$, 0.75, 1, 1.5, 2, 2.5, 3, 3.5, 4 U/a^2. The trajectories for the anticyclone are the same save for reflection about $y = 0$. The lower the value of β, the more the trajectories hug the coast (eastern boundary). Alternate curves are dashed to aid distinguishing them where they overlap.

Kloosterziel & van Heijst 1991 and Carnevale & Kloosterziel 1994). Unlike the case of the viscous rebound, where the strength of the anticyclone cannot grow once separation from the wall occurs, here the anticyclone can continue to increase in strength as the cyclone-anticyclone pair now moves to the northwest. This is evident in figure 4(*c,d,e*), and it is also evident that the vorticity in the cyclone decreases the further it propagates to the north. In later stages, as represented in panel (*f*), shedding of anticyclones is observed. This kind of vortex shedding has previously been observed in the propagation of vortices on a β-plane (far from boundaries) in laboratory experiments and simulations (Carnevale *et al.* 1991). The propagation to the northwest continues as long as the cyclone remains dominant. Long-term trajectories become complicated as the energy of the vortex radiates away into the Rossby wave field (the wave field supported by the β-effect). The failure of the vortices to return to the wall suggests that significant amounts of wall fluid may be transported away from the wall in this rebound process. This possibility is explored further in the next section.

We have repeated the simulation discussed here for a range of values of β without varying the initial values of the speed and radius of the modon. For each new β, the initial modon was redefined according to the dispersion formula (3.3) so that it would propagate without change except for the presence of the coast. In figure 5, we show the trajectories of vorticity extrema of the primary vortices for values of β from 0.5 to 4. Note that the distance that the primary vortex moves along the wall before separation decreases as a function of β.

We can make a model that approximately predicts the point of separation as a function of β. Let us concentrate on the motion of the cyclone. Separation will occur when the cyclone and accompanying anticyclone have moved sufficiently far north

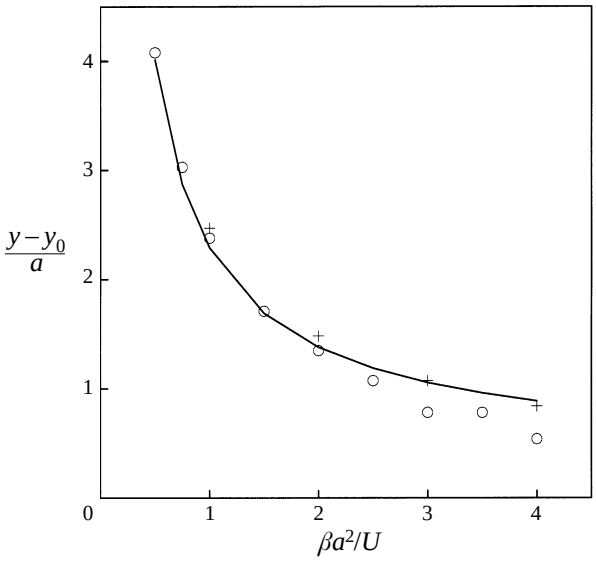

FIGURE 6. Graph of point of separation versus non-dimensional β. This plot shows the distance that the primary vortex travels along the wall before separation by one modon radius from the wall. The solid line shows the theoretical curve based on equation (3.7). The circles represent the results from finite-difference calculations, and the crosses those from vortex-in-cell simulations.

such that the anticyclone has gained sufficient strength to compete with the image vortex in the wall in regard to their effects on the trajectory of the cyclone. At the point of separation, the strength of the anticyclone will be some $O(1)$ fraction p of the strength of the cyclone. Since it is difficult to say much about the size or area of the vortices involved, we will use only the peak vorticity amplitudes to judge the strength of the vortices in this model. Thus, separation should occur when

$$|\omega_a| = p\omega_c, \tag{3.4}$$

where ω_a and ω_c are the peak amplitudes of the anticyclonic and cyclonic vorticity, respectively. By conservation of potential vorticity $\omega + \beta y =$ constant, and we have

$$\omega_c = \omega_0 - \beta(y - y_0), \tag{3.5}$$

and

$$\omega_a = -\beta(y - y_0), \tag{3.6}$$

where y_0 is the initial latitude of the peak of relative vorticity of the anticyclone and where we have neglected the difference between y_0 and the actual position of the initial peak of relative vorticity of the anticyclone. We have also neglected the relatively small initial value of ω_a. Thus at the point of separation,

$$y - y_0 = \frac{p}{1+p}\frac{\omega_0}{\beta}. \tag{3.7}$$

The combination ω_0/β is the so-called 'rest latitude' of the cyclone, that is, the maximum northward translation the cyclone could undergo while maintaining positive relative vorticity according to the law of potential vorticity conservation. With a and U fixed to be the same in all simulations, ω_0 is here a function of β as determined by the relations defining the modon, (3.2) and (3.3). In figure 6, we have plotted $y - y_0$ at separation as a function of β. Here we have defined the point of separation as

that position at which the peak vorticity in the cyclone has reached a distance of one modon radius a away from the wall. We have also plotted the relationship (3.7) (solid line) for a choice of p that gives the best least-square fit to the simulation data. The value of p for this fit is about 0.16. This provides a good measure of the value of the magnitude of the vorticity in the secondary vortex at separation only in the case of $\beta = 2$. For the other values, the actual percentage ranges from 0.05 to 0.25. Perhaps this mismatch indicates that a more complete theory must take into consideration the area of the anticyclone as well as its peak vorticity; however, results presented in the next section indicate that the area of the secondary vortex may not be a strong function of β. Other effects may be important. For example, note that when compared with the results from the finite-difference simulations, the model does best for low values of β. For the higher β values, there are additional vortices created as the primary vortex begins to rebound from the coast and these are not incorporated in the simple theoretical model.

We have repeated all of the numerical simulations in this section with an inviscid method, the vortex-in-cell method. In this numerical scheme, the vorticity distribution $\omega(x, y)$ is represented by a finite set of point vortices with circulations $\kappa_i = A\omega(x_i, y_i)$, where (x_i, y_i) is the position of the ith vortex, and A is the equal area represented by each point vortex. The vortices lie inside a rectangular region covered by a Cartesian mesh, on which the vorticity is calculated using the nine-point triangle-shaped-cloud scheme (TSC) (see e.g. Hockney & Eastwood 1981). The streamfunction is obtained by inverting the Poisson equation $\nabla^2\psi = \omega$ with the FACR (Fourier Analysis and Cyclic Reduction) method (Hockney 1970). The velocity field is evaluated from the streamfunction using a five-point centred differences scheme, and the velocity of each point vortex is determined with the same TSC interpolation factors used to obtain the vorticity on the grid. Finally, the positions of the point vortices are advanced in time using a second-order Runge–Kutta scheme, and the new relative vorticity is computed using the appropriate modulation equation, which, in the case of the quasi-geostrophic approximation, is

$$\kappa_i = \kappa_{0i} + A\beta(y_{0i} - y_i), \tag{3.8}$$

where κ_{0i} and y_{0i} are the initial circulation and position of the ith vortex.

The data from the vortex-in-cell method runs is represented by crosses in figure 6. It is not clear why those results correspond much more closely to the theory than do the high-β results for the finite-difference code. We tested the possibility of sensitivity to resolution of the finite-difference results by recomputing the $\beta = 4$ case with the finite-difference simulation at resolution 513×513 which is double the previous resolution. The results differed by less than 4%. Thus for the purposes of determining the separation point, the resolution for the finite-difference runs seems adequate. Also we checked the sensitivity of the results to the Reynolds number, and found that a 20% variation in Re produced a variation in the distance to separation of less than 0.5%. In any case, the finite-difference and vortex-in-cell methods agree sufficiently well for present purposes.

Although the physical bases for equations (2.1) and (3.1) are very different, in the early phase of the rebound they both rely on the development of oppositely signed vortices near the wall and the early behaviour shows some similarity. However, the subsequent evolution of the flow in the two cases is very different, as we have illustrated.

4. Fluid transport from the coast

Because we keep track of all particle positions (and velocities) during the whole flow evolution in the vortex-in-cell method, mass transport can be easily estimated by simply counting the number of particles that move from one region to another. We have decided, however, to do this calculation by accurately following the evolution of some selected regions of fluid. Numerically this is done by computing the motion of a set of nodes that define the boundaries of those regions. The number of nodes depends on both the length and the curvature of the contour, and it changes accordingly during the flow evolution. The area enclosed by any closed contour is a conserved quantity in this two-dimensional incompressible model; this provides a way to check the quality of the computation. In the simulations discussed below the areas are preserved to within 4%, even though the length of the contours may increase by a factor of 30.

We study how the mass transport towards and away from the wall depends on the gradient of background vorticity β, and on the modon inclination with respect to the wall. The values of β range from 0 to 4 in dimensionless units, whereas the inclination angle ranges from 0 to $\pi/4$. Other parameters such as the modon radius and speed have a fixed value of 1.

In the first series of simulations the modon moves perpendicularly to the wall from an initial distance of three modon radii. The transport of mass is evaluated by computing the evolution of the following contours: (*a*) the circular boundary of the modon, and (*b*) two straight lines parallel to the wall at distances $a/2$ and a, respectively (where a is the modon radius).

Figure 7 shows a representative example of the evolution of these contours. In frame (*a*), we see the initial conditions described above. Frames (*b*) and (*c*) show how the dipole displaces the wall fluid as it approaches the coast. Some of this fluid is wrapped around each dipole half (frame *d*) and is carried away from the coast as the dipole rebounds (frame *e*). Each dipole half forms a tripolar-like structure as it drifts away from the coast, with the core being formed by dipole fluid and the satellites by dipole and wall fluid (frame *f*). There is an accumulation of undyed fluid near the point on the wall where the dipole impact occurred (frame *f*). This undyed fluid was originally contained in two lobes in the region directly in front of the dipole in frame (*a*).

The same qualitative behaviour is observed in the whole range of β studied here. A quantitative comparison is made by computing the time evolution of the following areas: A_0, the area of modon fluid which is located at less than one modon radius from the wall; A_1, the area of the fluid which was initially located at less than one modon radius from the wall and which is currently located outside this band; and A_2 which is the same as A_1 but for a distance of half a modon radius. We chose the area of the modon as the unit of area.

The time evolution of A_0, A_1 and A_2 is shown in figure 8. The case $\beta = 0$ (lines without markers) is included as a reference. A_0 is zero initially because the modon lies completely outside the coastal region, but A_0 grows rapidly until it reaches a value of 1, with no further changes thereafter because the two dipole halves remain attached to the wall. Note that A_1 and A_2 can grow to values larger than 1, because they represent fluid displaced not only by the dipole fluid but also by any other fluid that intrudes into the near-wall region during the collision.

The curves corresponding to $\beta \neq 0$ show that, with increasing β, the maximum value of A_0, which is reached during the collision, decreases; the value of A_0 after the rebound, however, increases with increasing β. This means that for small β the dipole

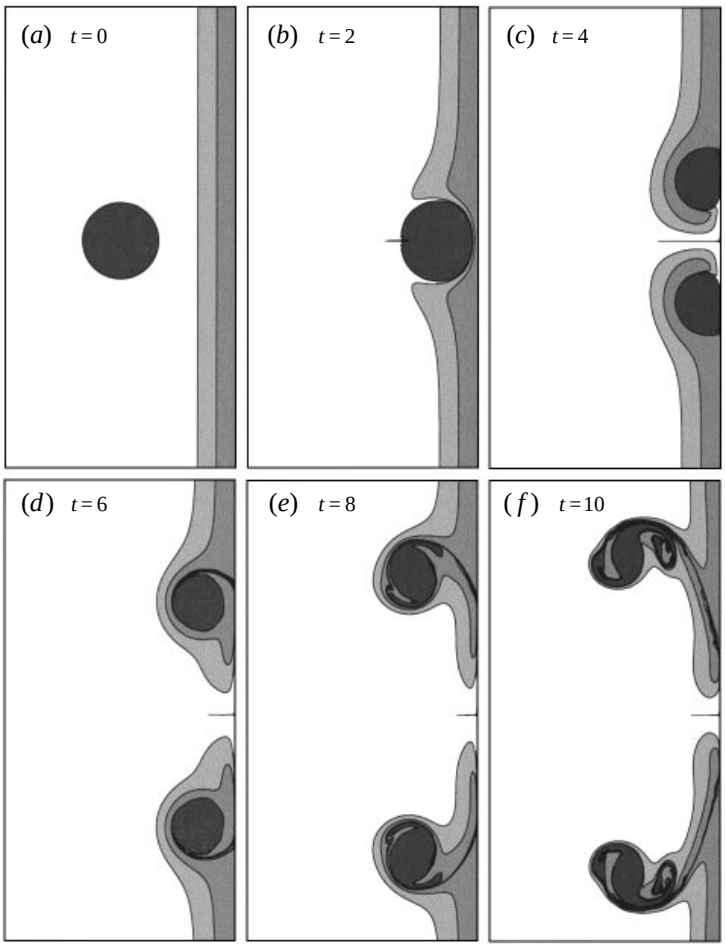

FIGURE 7. Contour plot of passive tracer from an inviscid simulation (vortex-in-cell method) of a modon colliding with a free-slip wall on the β-plane. The fluid which travels with the modon, that is, the fluid within the circle of radius a is coloured dark grey, and the fluid initially within one modon radius from the wall is coloured with two lighter shades of grey. In this simulation, $\beta = U/a^2$. The initial position of the modon was a distance of $3a$ from the wall. The size of the computational domain is $12.8a \times 12.8a$ of which only a portion of size $6a \times 12a$ is shown. The full computational domain consists of 128×128 cells each with initially 16 point vortices. The size of the time step is $0.005a/U$ and time is given in advective time units, a/U.

preserves most of its mass after the rebound, whereas for large β the dipole leaves a large fraction of its mass ($> 20\%$) within the coastal region. Figures 8(b) and 8(c) show that the area of fluid advected away from the wall decreases with increasing β, but it is always comparable to the initial modon area. Notice, however, that much of this fluid is not actually captured by the dipole (as is illustrated in figure 9) but is, instead, to be found in the wake of the vortex.

For values of β ranging from 1 to 4, the final amount of mass transported away from the wall region varies only by about 25%, while the point of detachment of the vortices changes by a factor 4 (cf. figure 6). Thus although the latitudinal range over which the displaced wall fluid is dispersed varies greatly with β, the total amount of that fluid does not.

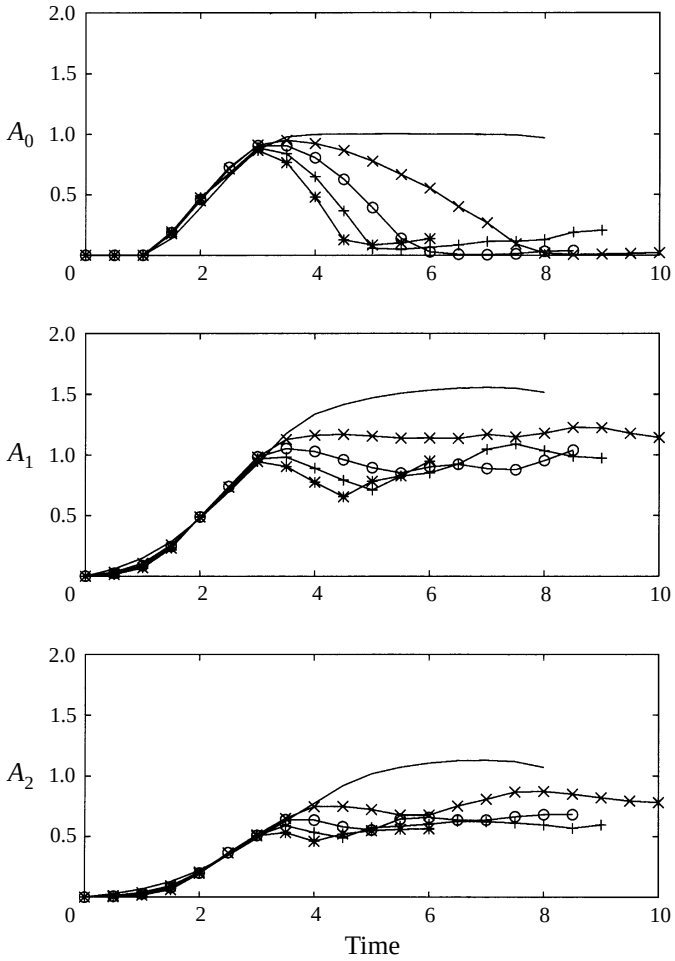

FIGURE 8. Graphs of mass transport during perpendicular collisions, for different values of β (0, no symbol; 1, crosses; 2, circles; 3, pluses; 4, asterisks). A_0 is the modon fluid entering the region within one modon radius from the coast. A_1 (A_2) represents boundary fluid that has left from the region within one (two) modon radius (radii) from the coast. Time is in advective time units (a/U), and areas are measured in units of the area within a circle of one modon radius.

We have also examined the sensitivity of the mass fluxes as a function of the angle of incidence. As the angle of approach (measured from the perpendicular direction) increases, the detachment distance (measured from the initial latitude) increases for one dipole half and decreases for the other. Therefore, the mass transport in the latitudinal direction is asymmetric. However, as seen from figure 10, the total area of fluid advected away from the wall is nearly independent of the angle of incidence and is roughly equal to the initial modon area for both regions 1 and 2.

5. Laboratory experiments

In physical applications, the formation of viscous boundary layers will always be possible at boundaries. Thus we must consider the competition between inviscid effects which may divert an approaching vortex before the effects of the viscous boundary layer become dominant and the viscous rebound effect. To this end, we

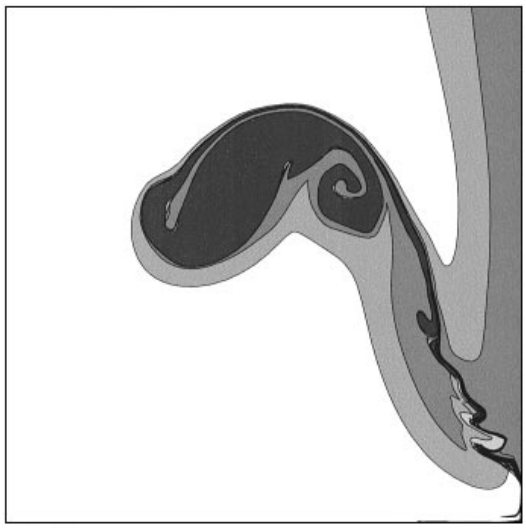

FIGURE 9. Contour plot of passive tracer from an inviscid simulation (vortex-in-cell method) of a modon colliding with a free-slip wall on the β-plane. The fluid which travels with the modon, that is, the fluid within the circle of radius a is coloured dark grey, and the fluid initially within one modon radius from the wall is coloured with two lighter shades of grey. The parameter values in this simulation were such that $\beta = 3U/a^2$. The initial position of the modon was a distance of $3a$ from the wall. The size of the computational domain is $12.8a \times 12.8a$ of which only a portion of size $5a \times 5a$ is shown. The full computational domain consists of 128×128 cells each with initially 16 point vortices. The size of the time step is $0.005a/U$ for this simulation, and the plot corresponds to time $t = 6.5\ a/U$.

performed a series of laboratory experiments in which dipoles collided with a wall in the presence of a β-effect. These experiments were carried out in a rotating cylindrical tank with a sloping bottom. A straight vertical wall was inserted on one side of the tank to act as the coastal boundary. The setup is shown in the schematic diagram in figure 11, which shows the view from above the tank, along the axis of rotation. The tank rotates at a fixed angular rotation rate, Ω. A bottom with uniform slope is used to mimic the β-effect. To understand how this works, we appeal to quasi-geostrophic theory. In this case, the inviscid behaviour is simply governed by the advection of potential vorticity, $q = \omega + h$ where h is proportional to the variation in the depth of the rotating fluid. Explicitly, we have $h = -f\Delta D/D$, where $f \equiv 2\Omega$, D is the mean depth of the fluid, and ΔD is a function of the horizontal coordinates, say x and y, and measures the variation of the depth from the mean. Thus if $\Delta D = -sy$ represents a constant slope with the shallower fluid at the top ('north') of our schematic, then $q = \omega + \beta y$, where $\beta = fs/D$. Thus, to the extent that the quasi-geostrophic approximation is valid, which is the case for sufficiently high rotation rates and sufficiently small depth variations, the inviscid part of the evolution is given again by equation (3.1). Also in the schematic, we have indicated a 'dipole generator' by the arrow on the left hand (topographic 'west') side of the tank. The dipole is created essentially by a jet of fluid into the tank. A detailed description of the dipole generator is given in Kloosterziel, Carnevale & Philippe (1993) and Carnevale & Kloosterziel (1994). The artificial coast is indicated in the schematic by the straight line on the right ('eastern') side of the tank. The dipole is generated in the 'west', propagates toward the 'east,' and then collides with the 'coast'.

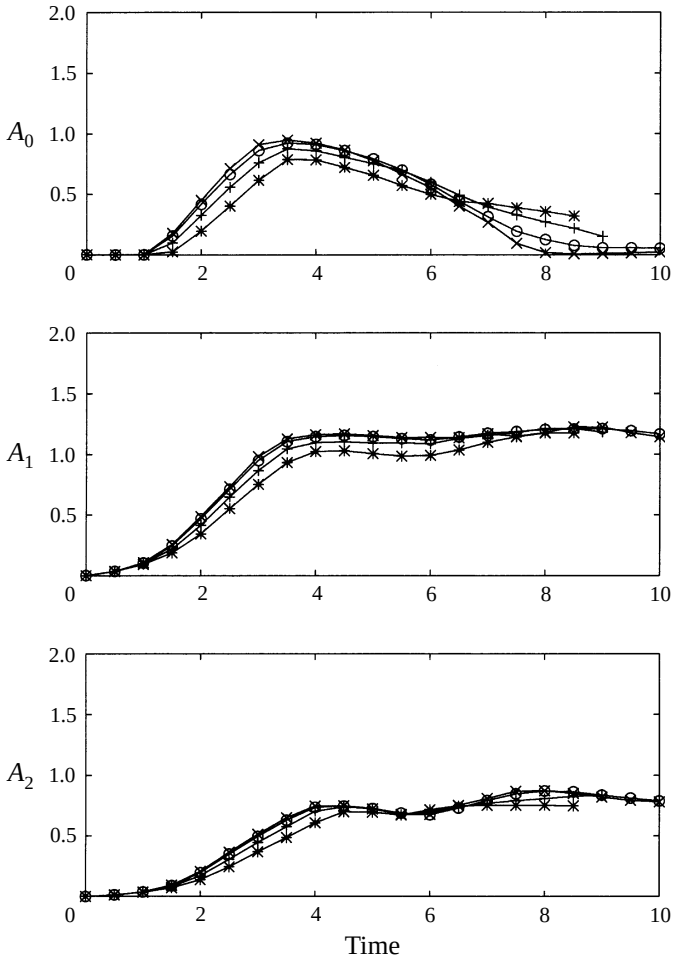

FIGURE 10. Same as figure 8 but now for a fixed value of β and varying tilting angle. Graphs of mass transport during oblique collisions, for different values of the angle of incidence (0, crosses; $\pi/12$, circles; $\pi/6$, pluses; $\pi/4$, asterisks).

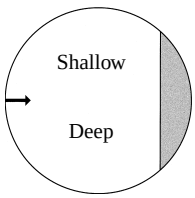

FIGURE 11. Schematic of rotating-tank apparatus. The view is from above, along the axis of rotation. Rotation is in the counter-clockwise sense from this point of view. The grey area is blocked from the flow by a vertical wall. The dipole is generated by a jet at the position of the arrow. The bottom of the tank has a constant slope with the shallower fluid toward the top of the figure.

In our experiments, the slope of the bottom and the speed and radius of the dipole were varied over a wide range in order to see both viscously dominated rebound and nearly inviscid rebound. An example of an experiment in which the β-effect dominated during rebound is shown in figure 12. As in the schematic, the view

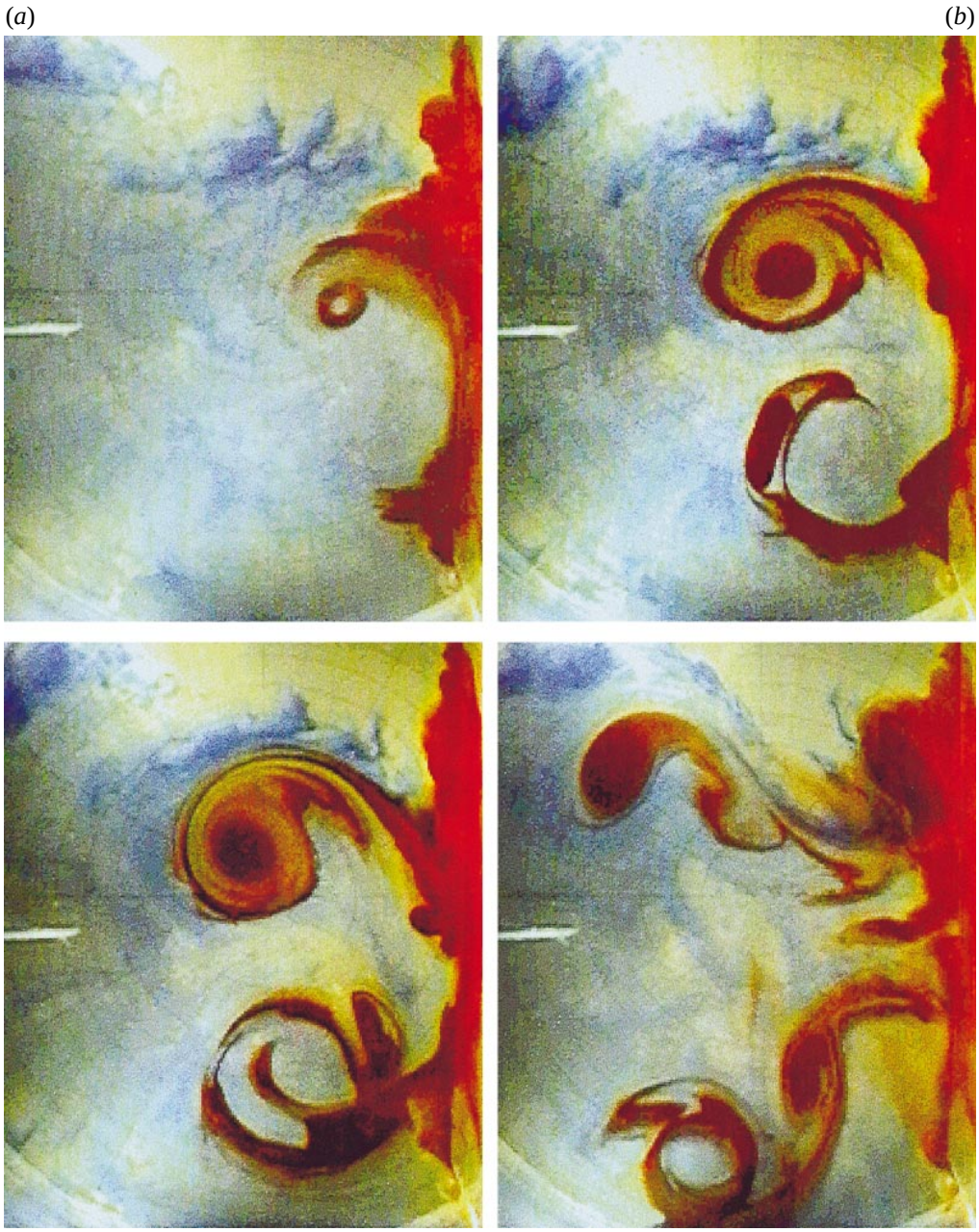

FIGURE 12. Dipole rebound in a rotating-tank experiment. The view is from above, and the camera is stationary in the rotating frame. The bottom of the tank has a constant slope with the shallower water toward the top of each frame, and the wall is on the right. A vertical plate that directs the jet from which the dipole is generated is seen as a bright straight line on the left of each figure. The initial velocity and size of the dipole are approximately $U = 1.4$ cm s^{-1} and $a = 17.5$ cm. The times represented are (*a*) 4 (*b*) 8, (*c*) 10, and (*d*) 14 in units of a/U. The panels show a portion of the tank measuring approximately 80 cm by 90 cm or $4.6a \times 5.1a$. The non-dimensional effective value of β given by the sloping bottom is $\beta_{nd} = 2.2$ (see text for further information).

is from above along the axis of rotation. The fluid toward the top/bottom of the image is shallow/deep. This orientation is such that the top/bottom of each image corresponds to the 'north'/'south' on the β-plane, while left and right correspond to 'west' and 'east' respectively. The bright straight line segment pointing toward the centre of the tank from the left edge of each frame indicates the source and direction of the jet that creates the dipole. The fluid is water with a mean depth of $D = 21$ cm and a bottom slope of $s = 0.18$. The period of rotation of the tank is 10.7 s. Thus the effective value of β is 0.01 $\text{cm}^{-1}\text{s}^{-1}$.

In order to visualize the action, we tried various methods for colouring portions of the flow. In the experiment illustrated in figure 12, the jet which forms the initial dipole and the background fluid were lightly dyed blue. The fluid at the wall was dyed red. In frame (*a*), although the dipole is not visible since its fluid is of the same colour as the background, we can begin to see its effects on the fluid at the wall (coast). Red-dyed fluid is pushed aside from the path of the dipole and begins to envelop the dipole as seen by the formation of the large semicircular arc of red-dyed fluid near the wall. Also note that red-dyed fluid is being drawn into the core of the cyclone of the dipole. This is a result of a secondary circulation within the vortex in which fluid is taken up into a cyclone by Ekman pumping (see Pedlosky 1987, p. 217). This vertical advection of the dye is a secondary effect of the Ekman pumping. The main effect is the decrease of vorticity amplitude and that can be incorporated in quasi-geostrophic theory by a linear decay law (cf. Pedlosky 1987). However, the vertical motions and the associated horizontal motions that transport the dye toward the centre of the vortex are not captured by quasi-geostrophic theory. This secondary effect also slowly pumps fluid downward and out of the anticyclone, so the core of the anticyclone remains relatively free of red dye during the course of the experiment. By frame (*b*), the cyclone and anticyclone are both visible (if only in outline for the anticyclone) and are now moving away from the wall. By the time of frame (*c*), it is clear that the β-effect is the dominating effect in this experiment since the vortices do not return to the wall and the evolution is very much as in the inviscid rebound discussed above. In frame (*d*), we see the well-developed wake of each of the primary vortices. These wakes are very similar to that observed when a single isolated vortex propagates on a β-plane as shown in Carnevale *et al.* (1991) and Carnevale & Kloosterziel (1994). Note that anticyclones/cyclones form near the primary cyclone/anticyclone, and these secondary vortices are then repeatedly left in the wake of the primary vortex.

In order to explore the competition between viscous and inviscid rebound mechanisms further, we produced a series of numerical simulations based on quasi-geostrophic dynamics with Laplacian dissipation. Thus the evolution in these simulations follows

$$\frac{\partial \omega}{\partial t} + J(\psi, \omega + \beta y) = \nu \nabla^2 \omega. \tag{5.1}$$

We did not include the familiar Ekman drag term, which would be necessary to make a quantitative comparison with the laboratory flows, because it is not essential to understanding the phenomenon in question, and makes no qualitative change to the behaviour. We performed a simulation with parameters chosen to be close to those observed in the laboratory experiment shown in figure 12. Measurements from the video film of this experiment suggests that the initial speed of the dipole is approximately $U = 1.4$ cm s^{-1} and the initial radius is about $a = 17.5$ cm. Thus, for this experiment, we have $\beta \approx 2.2U/a^2$. The flow was initialized with a Lamb

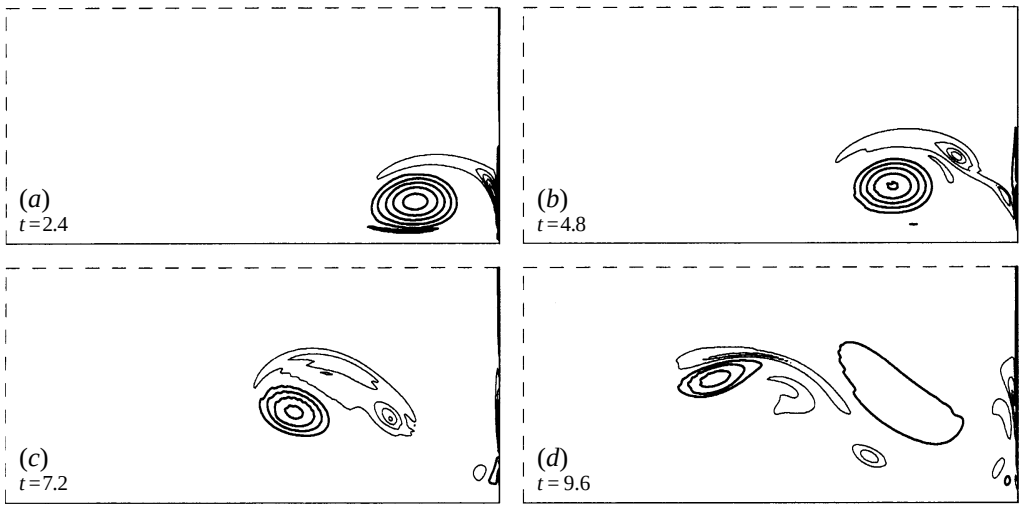

FIGURE 13. Vorticity contour plots illustrating the dipole rebound from a viscous no-slip boundary on a β-plane. Positive/negative vorticity contours are represented by thick/thin lines. The initial velocity and size of the dipole are approximately $U = 1.4$ cm s^{-1} and $a = 17.5$ cm. The times indicated are in advective time units a/U, and the vorticity contour interval is $0.625U/a$. The dimensions of the portion of the computational domain shown are 120 cm $\times$ 60 cm or approximately $6.9a \times 3.4a$. The Reynolds number $Re = Ua/\nu$ is 2450.

dipole placed 30 cm ($1.7a$) from the wall. The short time span and small spatial scales involved in the laboratory experiment, as well as the presence of viscous damping, prevent the dipole from reaching a perfect modon state before colliding with the wall. Thus, whether we represent it as a Lamb dipole or as a modon that has adjusted to the slope is probably of little consequence for these simulations. The resulting evolution is illustrated in figure 13. Only the evolution to the north of the symmetry line is shown since the motion to the south of this can be recovered by reflection with change of sign of vorticity. Initially, there is only a single cyclone north of the east-west symmetry line since the Lamb dipole has no side lobes. At time $t = 30$ s ($2.4\ a/U$), in addition to the boundary layer at the wall, we see that a lobe of anticyclonic fluid has formed to the north of the primary cyclone. The formation of the anticyclonic lobe, which is similar to the anticyclonic lobe to the north of the cyclone in the modon (see figure 3), results from the β-effect – zero-relative-vorticity fluid is advected to the north of the cyclone and, as a consequence of the conservation of potential vorticity, acquires negative relative vorticity. At time 60 s ($4.8\ a/U$), the strong side lobe has acquired relative vorticity both by the roll-up of wall vorticity and from the β-effect. As time progresses, the new dipole, formed of this side lobe and the original or primary cyclone, moves off on a northwest trajectory following the orientation of the new-dipole axis. As this dipole moves to the northwest, the anticyclone strengthens by the continued action of the β-effect, keeping the dipole from turning back toward the wall as it would if β were zero. As the evolution proceeds, there is some shedding of anticyclones. These shed anticyclones can give rise to additional cyclones by conservation of potential vorticity in the fluid advected locally around the anticyclone. As mentioned previously, this process of shedding anticyclones and subsequent additional cyclone formation creates the complicated wake typically observed in the long-term advection of a zero-circulation vortex on a β-plane (see Carnevale *et al.* 1991 and Carnevale & Kloosterziel 1994). By time

120 s = 9.6 a/U, a vortex wake has developed which is similar to that in the laboratory experiment shown in figure 12.

Based on the results of our laboratory and numerical simulations, we can infer that there are two basic regimes for dipoles rebounding from a no-slip wall on the β-plane. In the regime in which β is relatively large, the β-effect dominates and the dipole rebounds from the wall with the primary vortices moving away from the wall permanently, much as described in §3 above for inviscid flow. In the other regime, with β relatively small, viscous rebound dominates with behaviour like that described in §2, where the primary vortices return to the wall after the first rebound. We can try to estimate the values of the relevant parameters which would define these two regimes based on arguments given in §3. There we found that the distance that the primary vortex moves along the coast before separation due to the β-effect scales like $(\Delta y)_\beta \sim \omega_0/\beta$. If we then insert the relation $\omega_0 \sim U/a$ where U is the velocity of the dipole and a the radius of the dipole, then we have $(\Delta y)_\beta \sim U/(a\beta)$. Furthermore, as we discussed in §2, the distance the primary vortex travels along the wall for the pure viscous rebound problem is roughly independent of the magnitude of the viscosity and can be taken as $(\Delta y)_v \sim a$. Thus, if we say that the β-effect will dominate when the expected Δy is less that that due to viscous rebound, we have the following inequality:

$$(\Delta y)_\beta < (\Delta y)_v \tag{5.2}$$

or

$$\beta_{nd} > O(1), \tag{5.3}$$

where $\beta_{nd} \equiv a^2\beta/U$ is the value of β non-dimensionalized by the speed and radius of the modon. For example, in a series of experiments in which β and U are not varied, we would expect to find that viscous rebound dominates when a is small, while the β-effect should dominate for large a. The transition between the two behaviours should occur for $a = O(U/\beta)^{1/2}$. We have performed a series of simulations with fixed $U = 1$ cm s$^{1/2}$ and $\beta = 0.01$ cm s$^{1/2}$, and a in the range [5 cm, 20 cm]. These parameters were chosen to to be similar to those in the laboratory experiments that we performed. Equation (5.3) suggests a transition for $a = 10$ cm (i.e. $\beta_{nd} = 1$). In the simulation for $a = 20$ cm ($\beta_{nd} = 4$), the β-effect dominates, and the primary vortices never turn back toward the wall after the initial rebound. For $a = 5$ cm ($\beta_{nd} = 0.25$), the rebound seems very similar to pure viscous rebound, with the primary vortices repeatedly returning to the wall. For the intermediate value of $a = 10$ cm ($\beta_{nd} = 1$), the evolution is a fairly complicated combination of both behaviours. In that case, the early behaviour looks like viscous rebound, and the trajectories of the primary vortices do bend back toward the wall. However, the primary vortices do not quite make it all the way back to the wall, and in time the β-effect begins to dominate moving these vortices away from the wall. In this process, many secondary vortices are created, and there is significant Rossby radiation and viscous decay. Thus, it appears that our simple scaling rule (5.3) is of some use in predicting where the different regimes lie.

It is perhaps of interest to note that the formula for the length scale $a = (U/\beta)^{1/2}$ that marks the transition from viscous to β-induced rebound is very similar to that for the inverse Rhines wavenumber (Rhines 1975). The formula for the Rhines wavenumber is $k_\beta = (\beta/2u_{rms})^{1/2}$, where u_{rms} is the r.m.s. particle speed in a turbulent flow. This wavenumber determines the scale at which the mean Rossby wave phase speed is the same as the r.m.s. particle speed. It is a useful scale in discussing at which length scales wave motions or turbulent motions dominate the behaviour in β-plane

flow. Although our problem does not concern turbulent flow and our expression for the transition length scale was based on rather different considerations from those in Rhines (1975), there is a similarity nevertheless because we are determining when the β-effect will dominate over a process which is controlled mainly by the velocity and length scale of the flow (and not explicitly by ν). Thus, for dimensional reasons alone, one would expect the formula for the transition length scale to be very similar to that for the Rhines wavenumber.

We have not yet discussed a rather striking difference between the laboratory results shown in figure 12 and the numerical simulations. That difference is in the symmetry of the flows. In the laboratory experiment, there is a certain lack of symmetry, or more precisely antisymmetry, between the vorticity field in the 'north' compared to the field in the 'south'. According to the quasi-geostrophic equation, (5.1), if the dipole approaches the wall on a perpendicular axis, and the dipole is purely antisymmetric about that axis, then all subsequent motion must be antisymmetric. We can identify four possible reasons for the lack of pure antisymmetry in the laboratory experiments. The first is a lack of antisymmetry in the initial conditions – it is rather difficult to create a dipole that is perfectly antisymmetric initially and that will intersect the wall at right angles. A second effect may be the finite size of the deformation radius. In our experiments, the Rossby deformation radius was about 100 cm, which is about five times the radius of the dipole. Thus, it is unlikely that the finite deformation radius (which has been neglected in equation (5.1)) plays an important role. A third possible reason has to do with the decay rate of the vortices. Even on a flat plane, cyclones are expected to spin down more rapidly than anticyclones due to nonlinear Ekman effects (cf. Kloosterziel & van Heijst 1992). In our laboratory experiment the difference in decay rates is further increased by the different layer depths on the two sides of the tank. Since the cyclone is in shallower fluid that the anticyclone, the Ekman decay time, $H/(\nu\Omega)^{1/2}$, is smaller for the cyclone than for the anticyclone. We estimate that the decay time for the cyclone is about 30% less than that for the anticyclone. Nevertheless, since both decay times are less than the duration of the experiment, and more importantly because the cyclone travels faster than the anticyclone, we suspect another cause for the observed asymmetry. The fourth possibility can be understood in terms of considering how decreasing depth enhances the effects of a sloping bottom on the flow. If the variations in the topography are large, it is better to use shallow water theory in the simulations. On all fluid particles, evolution according to shallow water theory preserves the potential vorticity defined by

$$q = \frac{f + \omega}{H}, \tag{5.4}$$

where H is the depth of the fluid at the relevant point in the horizontal domain. We have a modified form of the vortex-in-cell code that obeys this more general form of the potential vorticity conservation. For the parameter values of relevance to our laboratory experiments, we find that simulations based on the shallow water equations do exhibit significant symmetry breaking due to this finite depth effect. An example of this symmetry breaking is illustrated in figure 14. Note that the effect of the slope on the cyclone seems to be more pronounced than for the anticyclone. In panel (f), we see that the cyclone has evolved more rapidly than the anticyclone in that it has moved farther from the wall and the secondary vorticity development is further advanced than in the case of the anticyclone. This makes sense in terms of the shallow water model because H is smaller in the vicinity of the cyclone than in the vicinity of the anticyclone. The local effective value of β could be written as $fs/\bar{H}$,

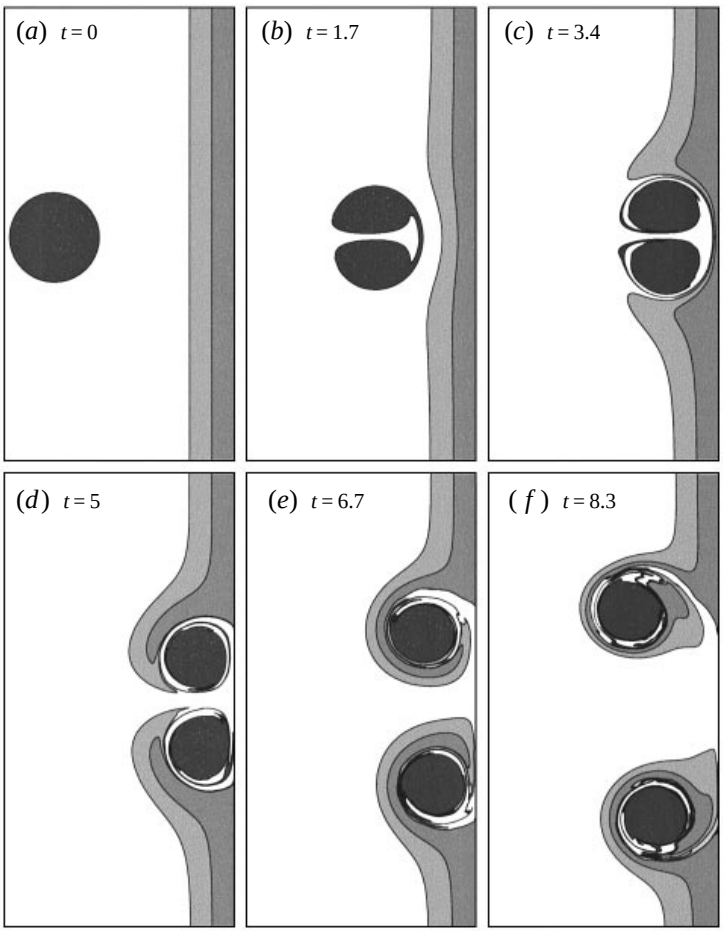

FIGURE 14. Inviscid simulation of a dipole colliding with a slip wall using the vortex-in-cell simulation for the shallow water model. The fluid which travels with the modon, that is, the fluid within the circle of radius a is coloured dark grey, and the fluid initially within one modon radius from the wall is coloured with two lighter shades of grey. The parameter values in this simulation were $s = 0.2$, $D = 33$ cm, $U = 1.5$ cm s^{-1}, and $a = 12.5$ cm, $f = 1.25$ s^{-1}. Thus the effective value of β is given by $\beta = 0.8U/a^2$. The initial position of the modon was a distance of $4a$ from the wall. The size of the computational domain is $12.8a \times 12.8a$ of which only a portion of size $5a \times 10a$ is shown. The full computational domain consists of 128×128 cells each with initially 16 point vortices. The size of the time step is $0.005a/U$. Time is given in advective time units, a/U.

where $\bar{H}$ is the mean value of the depth in the vicinity of the vortex in question. Thus this effective β will be stronger for the cyclone than for the anticyclone. We believe this is the primary explanation for the lack of perfect antisymmetry in the laboratory experiments where we see, as in figure 12, that the cyclone has moved farther away from the wall than the anticyclone.

6. Discussion

The study that we have presented is intended to establish some fundamental principles in regard to vorticity generation near a coast. Based on a particularly simple example, we have demonstrated that the β-effect can induce vortex rebound

and that, unlike the viscous rebound effect which typically does not produce a flux of wall fluid away from the wall, in the β-induced rebound the vortex carries coastal fluid into the interior, far away from the coast. Further, we established that it is the non-dimensional value of β that determines whether viscous or β-induced rebound will dominate. In terms of direct application to the ocean, eddies for which $\beta_{nd} \approx 1$, that is $(\beta a^2)/U \approx 1$, should show the intermediate behaviour in which both the β-effect and viscous rebound are important. If we take $U = 20$ cm s^{-1}, $a = 100$ km, and $\beta \approx 2 \times 10^{-13}$ cm^{-1} s^{-1}, we have $(\beta a^2)/U \approx 1$. Since these values are not atypical of eddies observed say in the California Current system (cf. Ramp *et al.* 1991 and Strub, Kosro & Huyer 1991), it seems that the effects of both viscous and β-driven rebound would be comparable there. On the other hand, effects of stratification and topographic variation may dominate both the β-effect and viscous boundary layer effects. In this regard, we can comment on the effect of a slope leading up to a coast in a barotropic flow; effects of stratification are outside the scope of the present work but certainly play a major role in coastal vortex rebound. We will consider the slope up to the coast to be uniform. Direct applicability will be limited since coastal topography is not usually this simple on the scale of meso-scale vortices. Looking at the magnitudes of slopes in the coastal region, we see that the slope on continental shelves typically corresponds to an effective β of the same order of magnitude as planetary β near mid latitudes. The slope in the 'slope' region is much more, however, and would dominate over the planetary β-effect in an purely barotropic flow. Wang (1992) presents a very detailed and interesting study of single vortices interacting with a continental slope. This interaction can produce a secondary topographic eddy that pairs with the primary vortex to produce a dipole which then interacts with the slope. There are other situations in which a study of dipoles propagating up a uniform slope toward a coast would perhaps also be a reasonable model. For example, consider the Gulf of Mexico, where the anticyclones that are shed from the Loop Current propagate westward and collide with the Mexican-USA coast. Along the coast not only are monopolar anticyclones observed, but there are cyclones which are found associated with the anticyclones in dipolar or even tripolar configurations (cf. Vidal *et al.* 1994). Furthermore, the slope of the bottom in the vicinity of the coast is fairly constant over large distances.

In previous studies, we have already considered the propagation of dipoles over an *unbounded* constant slope. These studies involved both laboratory and numerical experiments (cf. Carnevale *et al.* 1988*a*,*b*, and Kloosterziel *et al.* 1993). Basically, if the slope is not too strong, which would cause the dipole to break apart, then the dipole, originally pointing uphill, will turn toward the right and begin a oscillation about the contours of constant depth, moving in the mean in a direction which keeps shallow fluid on the left. In time, the oscillations damp out and the dipole moves along a trajectory following a constant-depth contour. This behaviour is entirely analogous to that of a modon on a β-plane if the initial orientation of the modon is not eastward (cf. Zabusky & McWilliams 1982; Carnevale *et al.* 1988*a*; Kloosterziel *et al.* 1993; Velasco Fuentes & van Heijst 1994).

If a coast is inserted parallel to the isolevels of the sloping bottom, the behaviour of the vortices becomes more complicated. We performed numerical simulations (both finite difference and vortex-in-cell) to investigate the basic behaviour of a dipole propagating upslope toward a coast. In one series of simulations, we initialized each experiment the same way, with the same Lamb dipole pointing directly at the coast and starting at the same distance from the coast. The dipole sits over a constant slope with depth contours aligned parallel to the coast. The slope extends indefinitely out

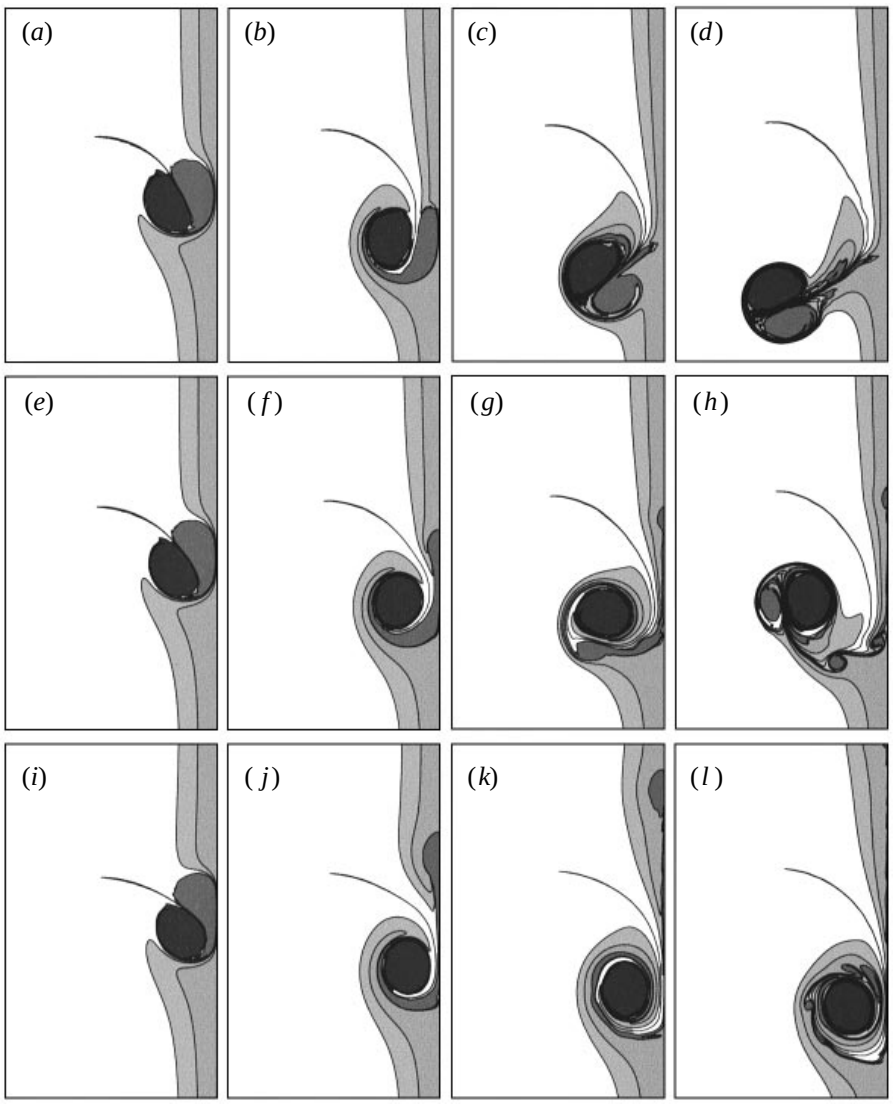

FIGURE 15. Grayscale plots of the evolution of different regions of fluid during the propagation of a dipole upslope toward a coast. The three rows of figures correspond to the evolution for 3 different values of the slope. The values of $\beta_{eff} = fs/D$ were 0.17, 0.15, and 0.11 U/a^2. Time proceeds from left to right in each row with the sequence of times given by $t = 5, 7, 9, 11\ a/U$. In each case the initial dipole is the Lamb dipole. The initial position of the dipole is $5a$ from the wall. The size of the computational domain is $12.8a \times 12.8a$ of which only a portion of size $5a \times 8.5a$ is shown. The full computational domain consists of 128×128 cells each with initially 16 point vortices. The size of the time-step is $0.005a/U$.

to sea. From one experiment to the next, we varied the magnitude of the slope. For a sufficiently strong slope, the dipole will not be able to approach the coast closely and the behaviour will be similar to that in the case of a slope with infinite extent. This is illustrated in the figure 15(*a–d*). In this figure, we do not show the initial dipole since it is the same in each case and is simply pointed toward the coast which is the right-hand border of each panel. The graphs are plots of material regions with different

shadings indicating different regions. As the dipole approaches the wall it turns to the right relative to its original direction of propagation. This is a result of conservation of potential vorticity. If we adopt coordinates with x increasing toward the coast (toward the right in the figure) y increasing toward the top of the figure, then, in the quasi-geostrophic approximation, the potential vorticity is $\omega + fsx/D$ where s is the slope and D is a mean depth which we could define as, for example, the depth at the midpoint between the dipole's initial position and the coast. As the dipole moves upslope, the strength of the cyclone decreases and the strength of the anticyclone increases. Thus, the anticyclone can pull the cyclone around in an arc, causing the dipole trajectory to bend to the right of its original direction. In figure 15(*a–d*), the dipole just grazes the coast, and will begin a series of oscillations that will damp and result in the dipole moving along a constant-depth contour parallel to the coast. In figure 15(*e–h*), the value of β has been reduced and the interaction with the wall is much stronger. Here we see that as the cyclone makes a close approach to the wall, it is torn into two pieces. This is due to the action of the shear field which results from the superposition of the field of the primary anticyclone and the image of the primary cyclone in the wall. This image is also an anticyclone, so the primary cyclone finds itself in a shear field as if it were between two anticyclones. After the cyclone is torn in two, one piece is dominated by its image vortex and moves along the coast away from the primary anticyclone. The other piece of the cyclone remains with the primary anticyclone. The strength of this cyclone is smaller than that of the anticyclone, and hence the basic motion is that of the cyclone revolving about the anticyclone. Superimposed on this motion is a gradual drift along the coast (in the negative y-direction) due to the interaction of the anticyclone with its image in the coast. If the slope is made stronger yet, then the presence of the wall can cause the primary cyclone to be separated almost entirely from the anticyclone as illustrated in figure 15(*i–l*). The result is a cyclone that moves along the wall in the y-direction and an anticyclone that moves along the coast in the opposite direction. The possibility, which one may reasonably consider, in which the anticyclone would propagate away from the wall (i.e. downslope) as suggested by the motion of an independent monopole on a slope (cf. Carnevale *et al.* 1991) has not been observed. We have attempted to find this behaviour by choosing to work with larger dipoles and stronger slopes, but to no avail. In each case that we tried, the anticyclone eventually moved along the coast following the isobaths. It seems that if the value of β is small enough so that the initial dipole can approach the wall sufficiently close to result in the separation of the two primary vortices, then the 'liberated' anticyclone is sufficiently close to the wall to form a stable dipole with its image vortex. Thus, the presence of a uniform slope alone will inhibit rebound in an inviscid flow.

An interesting detail in these simulations is the formation of small lobes of fluid in the moderate and weak slope cases as seen in figures 15(*h*) and 15(*l*). Such lobes are similar to those observed in the propagation of vortices on constant slopes as illustrated in Carnevale *et al.* (1991) and Carnevale & Kloosterziel (1994). Here they appear to be the result of an instability in the thin anticyclonic layer of fluid that is distributed around the cyclone.

In future work, we hope to look at the propagation of single vortices near coasts and to include the effects of stratification in a simple model.

This research has been supported in part by Office of Naval Research grant N00014-96-1-0065 and the University of Rome, 'La Sapienza.' O.U.V.F. is partially supported by CONACYT (Mexico) under grant 1890P-T. The numerical simulations

were performed on IBM workstations at the University of Rome and the University of San Diego, and on the C90 at the San Diego Super Computer Center. We thank Pedro Ripa for helpful comments and Robert Buffington for his help in the preparation of the colour figure.

REFERENCES

Arakawa, A. 1966 Computational design for long term numerical integration of the equations of fluid motion. *J. Comput. Phys.* **1**, 119–143.

Batchelor, G. K. 1967 *An Introduction to Fluid Dynamics*. Cambridge University Press.

Carnevale, G. F., Briscolini, M., Purini, R. & Vallis, G. K. 1988*b* Numerical experiments on modon stability to topographic perturbations. *Phys. Fluids* **31**, 2562–2566.

Carnevale, G. F. & Kloosterziel, R. C. 1994 Lobe shedding from propagating vortices. *Physica* D **76**, 147–167.

Carnevale, G. F., Kloosterziel, R. C. & Heijst, G. J. F. van 1991 Propagation of barotropic vortices over topography in a rotating tank. *J. Fluid Mech.* **233**, 119–139.

Carnevale, G. F., Vallis, G. K., Purini, R. & Briscolini, M. 1988*a* Propagation of barotropic modons over topography. *Geophys. Astrophys. Fluid Dynamics* **41**, 45–101.

Harvey, J. K. & Perry, F. J. 1971 Flow field produced by trailing vortices in the vicinity of the ground. *AIAA J.* **9**, 1659.

Heijst, G. J. F. van & Flor, J. B. 1989 Dipole formation and collisions in a stratified fluid. *Nature* **340**, 212–215.

Hockney, R. W. 1970 The potential calculation and some applications. In *Methods in Computational Physics. IX. Plasma Physics* (ed. B. Alder, S. Fernbach & M. Rotenberg), pp. 135–211. Academic.

Hockney, R. W. & Eastwood, J. W. 1981 *Computer Simulation using Particles*. McGraw-Hill.

Kloosterziel, R. C., Carnevale, G. F. & Philippe, D. 1993 Propagation of barotropic dipoles over topography in a rotating tank. *Dyn. Atmos. Oceans* **19**, 65–100.

Kloosterziel, R. C. & Heijst, G. J. F. van 1992 The evolution of stable barotropic vortices in a rotating free-surface fluid. *J. Fluid Mech.* **239**, 607–629.

Lamb, H. 1932 *Hydrodynamics*. Cambridge University Press.

Landau, L. D. & Lifshitz, E. M. 1959 *Fluid Mechanics*. Pergamon Press.

Larichev, V. D. & Reznik, G. M. 1976 Strongly nonlinear, two-dimensional isolated Rossby waves. *Oceanology*, **16**, 547–550.

McWilliams, J. C., Flierl, G. R., Larichev, V. D. & Reznik, G. M. 1981 Numerical studies of barotropic modons. *Dyn. Atmos. Oceans* **5**, 219–238.

Nycander, J. 1992 Refutation of stability proofs for dipole vortices. *Phys. Fluids* A **4**, 467–476.

Orlandi, P. 1990 Vortex dipole rebound from a wall. *Phys. Fluids* A **2**, 1429–1436.

Orlandi, P. 1991 Vortices interacting with nonslip walls: stirring and mixing of primary and secondary vorticity. *Phys. Fluids* A **3**, 1463.

Orlanski, I. 1976 A simple boundary condition for unbounded hyperbolic flows. *J. Comput. Phys.* **21**, 251–269.

Pedlosky, J. 1987 *Geophysical Fluid Dynamics*. Springer.

Pedlosky, J. 1996 *Ocean Circulation Theory*. Springer.

Peridier, V. J., Smith, F. T. & Walker, J. D. A. 1991 Vortex induced boundary layer separation. Part 1. The unsteady limit problem $Re \rightarrow \infty$. *J. Fluid Mech.* **232**, 99–131.

Peyret, R. & Taylor, T. D. 1983 *Computational Methods for Fluid Flow*. Springer.

Pond, S. & Pickard, G. L. 1978 *Introductory Dynamic Oceanography*. Pergamon.

Rai, M. M. & Moin, P. 1991 Direct simulations of turbulent flow using finite-difference schemes. *J. Comput. Phys.* **96**, 15–53.

Ramp, S. R., Jessen, P. F., Brink, K. H., Niiler, P. P., Dagget, F. L. & Best, J. S. 1991. The physical structure of cold filaments near Point Arena, California, during June 1987. *J. Geophys. Res.* **96**, 14859–14883.

Rhines, P. B. 1975 Waves and turbulence on a beta-plane. *J. Fluid Mech.* **69** 417–443.

Roache, P. J. 1982 *Computational Fluid Dynamics*. Hermosa.

Saffman, P. G. 1979 The approach of a vortex pair of a plane surface in inviscid fluid. *J. Fluid Mech.* **92**, 497–503.

Stern, M. E. 1975 Minimal properties of planetary eddies. *J. Mar. Res.* **33**, 1–13.

Strub, P. T., Kosro, P. M. & Huyer, A. 1991 The nature of the cold filaments in the California Current system. *J. Geophys. Res.* **96**, 14743–14768.

Velasco Fuentes, O. U. & Heijst, G. J. F. van 1994 Experimental study of dipolar vortices on a topographic β-plane. *J. Fluid Mech.* **259**, 79–106.

Vidal, V. M. V., Vidal, F. V., Hernandez, A. F., Meza, E. & Perez-Molero, J. M. 1994 Baroclinic flows, transports, and kinematic properties in a cyclonic-anticyclonic-cyclonic ring triad in the Gulf of Mexico. *J. Geophys. Res.* **99**, 7571–7597.

Wang, X. 1992 Interaction of an eddy with a continental slope. PhD Thesis, MIT/WHOI-92–40.

Zabusky, N. J. & McWilliams, J. C. 1982 A modulated point-vortex model for geostrophic, β-plane dynamics. *Phys. Fluids* **25**, 2175–2182.